

N₂ Electroreduction to NH₃ by Selenium Vacancy-Rich ReSe₂ Catalysis at an Abrupt Interface

Feili Lai, Wei Zong, Guanjie He, Yang, Xu, Haowei Huang, Bo Weng, Dewei Rao,* Johan A. Martens, Johan Hofkens, Ivan P. Parkin,* Tianxi Liu*

Dr. F. Lai, W. Zong, Prof. T. Liu

The Key Laboratory of Synthetic and Biological Colloids, Ministry of Education, School of Chemical and Material Engineering, Jiangnan University, Wuxi 214122, P. R. China

Email: txliu@jiangnan.edu.cn

Prof. J. Hofkens

Max Planck Institute for Polymer Research, Ackermannweg 10, 55128 Mainz, Germany

Dr. G. He, Dr. Y. Xu, Prof. I. Parkin

Christopher Ingold Laboratory, Department of Chemistry, University, College London, 20 Gordon Street, London WC1H 0AJ (UK)

E-mail: i.p.parkin@ucl.ac.uk

Dr. F. Lai, H. Huang, B. Weng, Prof. J. Hofkens

Department of Chemistry, KU Leuven, Celestijnenlaan 200F, Leuven 3001, Belgium

Prof. J. Martens

Centre of Surface Chemistry and Catalysis: Characterisation and Application team, KU Leuven, 3001 Leuven, Belgium

Dr. D. Rao

School of Materials Science and Engineering, Jiangsu University, Zhenjiang 212013, P. R. China

E-mail: dewei@ujs.edu.cn

Keywords: carbon nanofibers; COLSOM simulation; DFT calculations; nitrogen reduction reaction; ReSe₂

Abstract:

Vacancy engineering has been proved repeatedly as an adoptable strategy to boost electrocatalysis, while its poor selectivity restricts the usage in nitrogen reduction reaction (NRR) as overwhelming

competition from hydrogen evolution reaction (HER). Revealed by density functional theory calculations, the selenium vacancy in ReSe₂ crystal can enhance its electroactivity for both NRR and HER by shifting the d-band from -4.42 to -4.19 eV. To restrict the HER, we report a novel method by burying selenium vacancy-rich ReSe₂@carbonized bacterial cellulose (V_r-ReSe₂@CBC) nanofibers between two CBC layers, leading to boosted Faradaic efficiency of 42.5% and ammonia yield of 28.3 mg h⁻¹ cm⁻² at a potential of -0.25 V on an abrupt interface. As demonstrated by the nitrogen bubble adhesive force, superhydrophilic measurements, and COMSOL Multiphysics simulations, the hydrophobic and porous CBC layers can keep the internal V_r-ReSe₂@CBC nanofibers away from water coverage, leaving more unoccupied active sites for the N₂ reduction (especially for the potential determining step of proton-electron coupling and transferring processes as *NN → *NNH).

1. Introduction:

Ammonia (NH₃) is not only a vital feedstock to manufacture fertilizers, pharmaceutical and chemical products,^[1-3] but also a promising energy carrier with high hydrogen density and low liquefying pressure,^[4] making the fixation of the inexhaustible nitrogen (N₂) into NH₃ a key transformation. However, N₂ fixation is still severely confined by the thermodynamic stability of the N₂ molecule and the absence of a permanent dipole in the N≡N triple bond.^[5,6] As a century-old N₂ fixation method, the Haber–Bosch process occupies an important industrial position in NH₃ manufacture, which requires both iron-based catalysts and harsh operating conditions (400-600 °C and 150-350 atm).^[7] As a consequence, 1.4% of the world’s energy consumption is used in the Haber-Bosch process, leading to 1.6% of total global CO₂ emission,^[8,9] which makes the exploration of sustainable N₂ fixation systems under ambient conditions an important issue.^[10,11]

Electrochemical N₂ reduction reaction (NRR) emerges as an alternative technology to fix nitrogen into ammonia at ambient conditions.^[12-14] This can be powered by renewable energy from electrochemical cells and operate by using versatile hydrogen atoms as alternative sources.^[15,16] Until

now, the development of NRR is mainly focused on exploring advanced electrocatalysts to activate dinitrogen for alleviated energy barriers.^[17,18] Among them, transition metal based electrocatalysts are regarded as promising species towards the NRR process,^[19-23] due to their available d-orbital electrons for π -back donation process. However, their practical applications are still hindered by low NH_3 yield and Faradaic efficiency, which originates from the following two perspectives: (1) the binding force between transition metals and nonpolar dinitrogen is too weak to break the strong $\text{N}\equiv\text{N}$ triple bond due to the poorly optimized structure of the electrocatalyst;^[24] (2) the adverse hydrogen evolution reaction (HER) is regarded as an intense-competing reaction towards NRR due to the preferential adsorption of the hydrogen (H) atom over a nitrogen (N) atom.^[8,25] For an enhanced interfacial force towards nitrogen, one effective strategy is to tailor the electronic structure of the transition metal based electrocatalysts by incorporating defect structures (such as anionic vacancies). The existence of anionic vacancies may change the charge distribution and activate the transition metals near the vacancies, leading to an increased number of active sites for enhanced NRR process with stronger N-metal interaction. For instance, Sun et al. found that the defect-rich transition metal dichalcogenide MoS_2 with a flower-like structure shows outstanding electrocatalysis for N_2 reduction to NH_3 , as compared to the defect-free counterpart.^[23] However, the as-incorporated defect structures may also be beneficial for achieving a stronger proton-metal interaction for an accelerated HER process.^[26,27] This reaction is an intense competitor towards NRR, and hence would significantly decrease the effective number of active sites for N_2 adsorption and activation. Recently, Ling et al. designed a new NRR electrocatalyst by introducing a superhydrophobic layer of zeolitic imidazolate framework-71 over the surface of a NRR electrocatalyst, which realized a significant boost in Faradic efficiency (10 percent increase) by suppressing the HER process.^[25] Therefore, it becomes a key issue in combining defect engineering (such as anion vacancies) in transition metal-based electrocatalysts with an optimized three-phase boundary, but not changing the N_2 transmission to the defect-rich surface and reducing its number of active sites for N_2 adsorption/activation.

Herein, we report an efficient and selective NRR process under ambient conditions by sandwiching selenium vacancy-rich ReSe_2 @carbonized bacterial cellulose ($\text{V}_r\text{-ReSe}_2\text{@CBC}$) nanofibers between two hydrophobic CBC layers. Density functional theory (DFT) calculations demonstrate that defect engineering could enhance the electrocatalytic properties of ReSe_2 by positively shifting its d-band center but show poor selectivity towards nitrogen reduction and hydrogen evolution reactions. Interestingly, the competition from HER process can be suppressed by covering hydrophobic CBC layers on both sides of $\text{V}_r\text{-ReSe}_2\text{@CBC}$ nanofibers, resulting in a boosted Faradaic efficiency of 42.5% and a maintained NH_3 yield of $28.3 \text{ mg h}^{-1} \text{ cm}^{-2}$ at room temperature. The detailed advantages for the “sandwich”-structured $\text{CBC/V}_r\text{-ReSe}_2\text{@CBC/CBC}$ membrane were further unveiled by under-electrolyte nitrogen bubble adhesive force tests, contact angle measurements, and COMSOL Multiphysics simulations from experimental and theoretical approaches.

2. Results and Discussion:

The selenium vacancy-rich rhenium diselenide nanosheets were anchored on the surface of carbonized bacterial cellulose nanofibers (Figure S1 & S2) by combining hydrothermal synthesis and heat treatment (Ar gas, $700 \text{ }^\circ\text{C}$ for 3 h; Figure 1a), denoted as selenium vacancy-rich $\text{ReSe}_2\text{@CBC}$ ($\text{V}_r\text{-ReSe}_2\text{@CBC}$) nanofibers (NFs). In comparison, vacancy-poor $\text{ReSe}_2\text{@CBC}$ ($\text{V}_p\text{-ReSe}_2\text{@CBC}$) NFs were prepared by annealing hydrothermally-synthesized $\text{ReSe}_2\text{@CNC}$ NFs under a Se-rich atmosphere. The transmission electron microscopy (TEM) image for $\text{V}_r\text{-ReSe}_2\text{@CBC}$ NFs (Figure 1b) exhibits abundant nanofibrous integrities with diameters of $\approx 30 \text{ nm}$. According to this hybridization strategy, the $\text{V}_r\text{-ReSe}_2\text{@CBC}$ NFs would deliver a higher specific surface area of $55.4 \text{ m}^2 \text{ g}^{-1}$ and abundant micro-/mesopores from the nitrogen physisorption isotherms (measured at $-196 \text{ }^\circ\text{C}$) and pore sizes distributions (Figure S3), as compared to that of $9.8 \text{ m}^2 \text{ g}^{-1}$ for ReSe_2 bulk with abundant aggregations (Figure S4). As clearly shown by the high-resolution TEM (HRTEM) image in Figure 1

c, the amorphous CBC NFs provide a one-dimensional matrix to physically and uniformly connect highly crystalline V_r -ReSe₂ nanosheets with a fringe spacing of 0.64 nm, corresponding to the (100) plane of ReSe₂ (Inset image in Figure 2c for V_r -ReSe₂ model). It should be noted that the V_p -ReSe₂ nanosheets in V_p -ReSe₂@CBC NFs also possess the same fringe spacing of 0.64 nm as V_r -ReSe₂ nanosheets in V_r -ReSe₂@CBC (Figure S5), which indicates the slightly incorporated selenium vacancy in ReSe₂ would not obviously affect its crystal structure. The similar X-ray diffraction (XRD) patterns between V_r -ReSe₂@CBC and V_p -ReSe₂@CBC NFs (Figure S6) prove the results from HRTEM images with optimal crystal orientation of (100) plane. Specifically, six peaks at 13.3°, 31.4°, 36.4°, 42.4°, 47.1°, and 55.6° can be well indexed to the (100), (-102), (102), (300), (003), and (-421) planes for both V_r -ReSe₂ and V_p -ReSe₂ nanosheets (JCPDS: 18-1086). The TEM and corresponding energy-dispersive X-ray (EDX) elemental mapping images (Figure 1d) further demonstrate the uniform distribution of Re and Se elements along the CBC nanofibers. The EDX spectrum (Figure S7) reveals the existence of Re, Se, and C elements in V_r -ReSe₂@CBC NFs, which can also be proved from the successful appearance of Re, Se, and C peaks (Figure S8 & Figure 1e) in X-ray photoelectron spectroscopy (XPS).

To confirm the incorporation of selenium vacancies in V_r -ReSe₂@CBC NFs and gain the information of local chemical environments of as-prepared materials, XPS, electron paramagnetic resonance (EPR), and synchrotron radiation technology measurements were conducted. From the XPS results firstly, two obviously characteristic peaks can be observed at 42.1 and 44.4 eV in the Re 4f region (Figure S8b), corresponding to the core 4f_{7/2} and 4f_{5/2} peaks for Re⁴⁺, respectively.^[28] The visible Se region at 55.2 eV (Figure 1 e) strongly confirms the formation of ReSe₂. In addition, the Se 3d peak of V_r -ReSe₂@CBC NFs displays a negative shift of 0.2 eV to relatively lower binding energy value as compared to that of V_p -ReSe₂@CBC NFs, while there is no discernible variation in Re 4f peaks. These XPS results indicate the electron density around Se atoms is slightly increased after heat treatment under Ar gas, demonstrating the successful introduction of selenium vacancies without

cationic ones. Meanwhile, the EPR investigations were applied to verify the existence of selenium vacancies within $V_r\text{-ReSe}_2$ nanosheets as such defects in semiconductors are usually paramagnetic.^[29] As displayed in Figure 1 f, the EPR signal at $g=2.002$ for the $V_r\text{-ReSe}_2$ nanosheets is caused by the trapped electrons from the selenium vacancies,^[30-32] while a much lower signal can be observed for the $V_p\text{-ReSe}_2$ nanosheets at the same position, demonstrating abundant selenium vacancies have been successfully incorporated into $V_r\text{-ReSe}_2$ nanosheets. Furthermore, the X-ray absorption fine structure (XAFS) spectroscopy confirms the existence of selenium vacancies. Generally speaking, the intensity of Re L_3 -edge curve from soft X-ray absorption near-edge structure (XANES) spectroscopy is mainly depended on the nearest neighbor cation-anion bond and the number of electrons in the unoccupied state.^[33-35] As the Re L_3 -edge XANES spectra shown in Figure 1g, the obvious difference between the curves of $V_r\text{-ReSe}_2$ and $V_p\text{-ReSe}_2$ nanosheets indicates that the structural symmetry in $V_r\text{-ReSe}_2$ nanosheets has been partially disturbed with decreased coordination number after the incorporation of selenium vacancy. Fourier transform (FT) is a basic method for the data extraction and interpretation of EXAFS spectra.^[36] The FT-EXAFS spectra of $V_p\text{-ReSe}_2$ and $V_r\text{-ReSe}_2$ nanosheets were illustrated in Figure 1h. The peak position of the corresponding Re-Se coordination for $V_r\text{-ReSe}_2$ nanosheets is slightly shifted to a higher Radial distance (2.11 Å) as compared to the $V_p\text{-ReSe}_2$ nanosheets (2.06 Å) (Figure 1 h), indicating the Re-Se bond length in $V_r\text{-ReSe}_2$ nanosheets is slightly increased after incorporating selenium vacancies. In addition, the peak intensity of $V_r\text{-ReSe}_2$ nanosheets decreases slightly as compared to the $V_p\text{-ReSe}_2$ nanosheets (Figure S9). Therefore, it is proved once more that the selenium vacancies in $V_r\text{-ReSe}_2$ nanosheets would cause structural distortion,^[37,38] where the detailed structure parameters are summarized from the curve fitting in Table S2 (Supporting Information). The Re-Se bond in the $V_r\text{-ReSe}_2$ nanosheets exhibit unsaturated coordination with lower coordination number (N) of 5 as compared to the $V_p\text{-ReSe}_2$ nanosheets (N=6), which is resulted from the removal of partial Se sites from the basal plane of ReSe_2 nanosheets. As a very good supplement for FT, wavelet transform (WT) possesses power resolution in both k and R spaces.^[39] The WT contour

plots for both V_p -ReSe₂ and V_r -ReSe₂ nanosheets (Figure 1i & S10) display intensity maximums at $\approx 8.6 \text{ \AA}^{-1}$, indicating only one Re-Se ligand can be found at the same time without any incorporated impure ligands during preparation process.

Upon confirming the successful synthesis of V_r -ReSe₂@CBC NFs, we firstly evaluated the performance of perfect ReSe₂ and its Se vacancy one (V-ReSe₂) through density functional theory (DFT) calculations with detailed calculation methods in the Supporting Information. The electronic structures of ReSe₂ and V-ReSe₂, as well as their electrocatalytic steps for both NRR and HER, were calculated as displayed in Figure 2 & S11. The plots of total density of state (DOS) are shown in Figure 2a, from which the d-band centers for V-ReSe₂ and ReSe₂ are calculated to be -4.19 and -4.42 eV, respectively. It indicates the strong interaction between N₂/H₂O and V-ReSe₂ surface, due to more electrons distributing around Fermi level. Then, the electrons can be easily transferred to N₂/H₂O with enhanced adsorption ability of V-ReSe₂ toward N₂/H₂O. Additionally, the electrons of perfect surface are mainly located between Se and Re, which can be verified by the accumulated electrons (pink color area in the inset of Figure 2 a) between Re and Se with the missing of one Se on V-ReSe₂, indicating that the electrons on perfect surface are localized and more delocalized on V-ReSe₂. And the delocalized electrons are readily excited to the conduction band, leading to its enhanced conductivity and the activation ability towards N₂ and H₂O molecules for accelerated NRR and HER processes. As revealed by previous reports (Figure S12),^[23] three different reaction pathways are suggested for NRR, which are heavily depended on the adsorption of N₂. Hereon, the adsorption behavior of N₂ were explored, and we found that the N₂ was likely side-on adsorbed on ReSe₂ and distorted end-on adsorption on Se-vacancy sites (Figure S13 & S14). Therefore, the enzymatic mechanism of NRR processes for ReSe₂ and distal and alternating pathways for V-ReSe₂ are suggested and studied. As shown in Figure 2b, the optimized NRR processes, enzymatic pathway for ReSe₂ and alternating pathway for V-ReSe₂, in the form of free energy diagrams are displayed (more details of energy data are filled in Table S3), as well as their geometric structures (more details of structures are shown in

Figure S13 & S14, and coordinates of all structures are shown in the last section of the Supporting Information). Obviously, the free energy for N₂ adsorption on ReSe₂ is much higher than it on V-ReSe₂, suggesting that the N₂ would be more active on V-ReSe₂, which can help to accelerate the NRR processes. Specially, for V-ReSe₂, the free energy levels are all lower than the pathway of N₂ reduction on ReSe₂. In terms of distal pathway on V-ReSe₂, based on DFT calculations, the *NNH₂ is not the energetically preferred intermediate, for which the total energy is 0.76 eV higher than that of *HNNH. Consequently, the promising reaction mechanism for N₂ on V-ReSe₂ is the alternating pathway. These calculation results reveal the incorporated Se vacancy would activate the V-ReSe₂ catalyst with a highly accelerated NRR process as compared with the vacancy-free ReSe₂ catalyst. However, Se vacancy is also found to be effective in promoting the HER process, an intense-competing reaction towards NRR, for the V-ReSe₂ catalyst (Figure 2c). The free energy value is 1.45 eV for ReSe₂ catalyst, far away from the optimal value ($\Delta G_{*H} = 0$ eV), and the water adsorption energy is also as high as 0.61 eV, which means that the dissociation of water is very difficult, resulting in the sluggish HER kinetics. After the incorporation of the Se vacancy, the free energy of water adsorption is dramatically reduced to 0.02 eV at the surface of the V-ReSe₂ catalyst. Meanwhile, the ΔG_{*H} value for V-ReSe₂ catalyst is also shifted to -0.39 eV, demonstrating it is thermodynamically favorable for *H reduction. As a consequence, the theoretical analysis reveals the pure vacancy engineering is not an ideal strategy for the design of NRR catalyst due to its poor selectivity between simultaneously promoted NRR and HER processes.

Furthermore, the theoretical calculation results are also proved from the following experimental results, where V_r-ReSe₂@CBC and V_p-ReSe₂@CBC are used as electrocatalysts towards both NRR and HER processes. Based on three calibration curves for NH₃ detection by using indophenol blue, high-performance ion chromatography (HPIC), and nuclear magnetic resonance (NMR) methods (Figure S15), the ammonia contents in 0.1M Na₂SO₄ electrolyte produced from nitrogen reduction reaction were analyzed as average values from the results of ultraviolet (UV) peaks, HPIC areas, and

nuclear magnetic resonance signals. In addition, a series of blank experiments were conducted to check the purity of 0.1M Na₂SO₄ electrolyte (Figure S16), applied N₂/Ar gases (Figure S17), and ¹⁵N₂ gas (Figure S18), which all show no NH₃ contamination. By employing V_r-ReSe₂@CBC and V_p-ReSe₂@CBC NFs as the cathodic catalysts, the potentiostatic NRR tests were measured with continuous N₂ bubbling at ambient conditions. As shown in Figure 3a, the highest average NH₃ yields and corresponding Faradaic efficiencies (FEs) of V_r-ReSe₂@CBC NFs are achieved at -0.2 V versus reversible hydrogen electrode (RHE), reaching approximately 41.9 mg h⁻¹ cm⁻² and 10.2%, respectively, which are much higher than those of V_p-ReSe₂@CBC NFs (7.9 mg h⁻¹ cm⁻², FE=6.1%). The enhanced NRR performance of V_r-ReSe₂@CBC NFs is attributed to its activated electronic structure after introducing abundant Se vacancies, which displays enhanced adsorption/dissociation ability towards N-related groups (Figure 2 b). As the potential gets lower than -0.2 V, the NH₃ yields and Faradaic efficiencies decrease significantly due to the overwhelming competition from the HER process, while their decrease at a more positive potential of -0.1 V is originated from the limited electron to reduce N₂ into NH₃ production. In order to exclude other possibilities of NH₃ contaminations, such as N-contained precursor/solvent (NH₂OH·HCl/hydrazine hydrate) during the synthetic process, another two blank experiments were also conducted (Figure S19). In addition, the CBC nanofiber shows negative NRR performance (Figure S20), and only acts as a one-dimensional matrix to provide uniform distribution of V_r-ReSe₂ nanosheets for enhanced charge transfer ability, leading to higher NH₃ production as compared with the corresponding bulk (Figure S21). The outstanding performance of as-obtained V_r-ReSe₂@CBC NFs is comparable with the NH₃ yields and Faradaic efficiencies of previous electrocatalysts (Table S4). Meanwhile, no hydrazine is detected in the electrolyte (Figure S22), proving the high selectivity of V_r-ReSe₂@CBC NFs. As displayed in Figure S23, both the average NH₃ yields and Faradaic efficiencies maintain at a stable level without obvious fluctuation, which demonstrates good potential for industrial applications of the catalysts. However, the V_r-ReSe₂@CBC NFs also show an enhanced electrocatalytic performance towards

hydrogen evolution reactions (Figure S24), which matches well with the DFT calculation results (Figure 2c). In detail, the $V_r\text{-ReSe}_2\text{@CBC}$ NFs show lower onset overpotential ($\eta = 178$ mV) and Tafel slope (75 mV dec^{-1}) than those for $V_p\text{-ReSe}_2\text{@CBC}$ NFs ($\eta = 245$ mV; Tafel slope: 85 mV dec^{-1}), demonstrating the positive role of selenium vacancy towards hydrogen evolution reactions.

Therefore, vacancy engineering is revealed as an underutilized strategy with poor NRR selectivity, which would boost not only NRR but also HER processes from both theoretical and experimental results. In order to suppress competing HER and increase the Faradaic efficiency for NRR, a “sandwich”-structured $\text{CBC}/V_r\text{-ReSe}_2\text{@CBC}/\text{CBC}$ membrane was constructed by encapsulating $V_r\text{-ReSe}_2\text{@CBC}$ NFs between two hydrophobic CBC layers (Figure 3b) after filtering CBC, $V_r\text{-ReSe}_2\text{@CBC}$, and CBC suspensions via a layer by layer process (mass ratio for the three components is 1:1:1). The prepared $\text{CBC}/V_r\text{-ReSe}_2\text{@CBC}/\text{CBC}$ membrane is displayed in Figure S25, which possesses extraordinary flexibility as an electrode for nitrogen reduction reactions. As the EDX elemental mapping images of its cross-section shown in Figure 3c, the $V_r\text{-ReSe}_2\text{@CBC}$ NFs are uniformly buried under the coverage of two-side hydrophobic CBC layers. The CBC layers make it possible to achieve a hydrophobic interior of $V_r\text{-ReSe}_2\text{@CBC}$ with trace vaporized water, thus impeding HER process with reduced Faradaic efficiency. Consequently, abundant humid N_2 gas would infuse into the $V_r\text{-ReSe}_2\text{@CBC}$ NFs and concentrate near its surface driven by the thermodynamically favorable sorption,^[40] leading to the enhanced NRR process with possibly high Faradaic efficiency.

As displayed in Figure 4a, the highest average NH_3 yield and corresponding Faradaic efficiency for $\text{CBC}/V_r\text{-ReSe}_2\text{@CBC}/\text{CBC}$ membrane are achieved to be 28.3 mg h^{-1} cm^{-2} and 42.5%, respectively, when the negative potential reaches to -0.25 V. The four-fold increase in Faradaic efficiency for NRR can originate from the anti-hydrogen evolution reaction with the existence of two-side hydrophobic CBC layers (Figure 3d), making more supplied electrons to reduce nitrogen molecules. Additionally, the impeded HER process in $\text{CBC}/V_r\text{-ReSe}_2\text{@CBC}/\text{CBC}$ membrane can also be proved from its significantly reduced current density, negatively shifted onset overpotential, and higher Tafel slope as

compared with those for $V_r\text{-ReSe}_2\text{@CBC}$ NFs (Figure S26). As the potential is more negative than -0.25 V, both the NH_3 yield and Faradaic efficiency decrease continuously, as the hydrophobicity of $\text{CBC}/V_r\text{-ReSe}_2\text{@CBC}/\text{CBC}$ membrane is changed into a hydrophilic character under high negative voltage according to previous reports,^[41] thus leading to the revitalization of hydrogen evolution reaction as an overwhelming competition. Although the NH_3 yield at -0.15 V decreases to $3.2 \text{ mg h}^{-1} \text{ cm}^{-2}$ sharply (due to the limited electron to reduce N_2 into NH_3), the Faradaic efficiency still maintains at a high level of 35.3% attributing to the excellent hydrophobicity of CBC layer at this potential. In spite of ruling out the possible NH_3 contaminations from the electrocatalyst itself (Figure S19), a ^{15}N isotopic labeling experiment (Figure 4b) was further used to confirm the ammonia production. The ^1H NMR spectra of commercial $(^{14}\text{NH}_4)_2\text{SO}_4$ and $(^{15}\text{NH}_4)_2\text{SO}_4$ samples were collected as standard spectra. In particular, the ^1H NMR spectra for the electrolytes after the electrocatalytic process at -0.25 V show a ^{14}N triplet ($I = 1$) and a ^{15}N doublet ($I = 1/2$) in the range of 6.85-7.15 ppm, respectively. The peak positions for both triplet and doublet closely match the reference substance of $(^{14}\text{NH}_4)_2\text{SO}_4$ and $(^{15}\text{NH}_4)_2\text{SO}_4$, thus demonstrating the successful production of ammonia during the NRR process. Additionally, when $^{15}\text{N}_2$ gas was used as a feedstock, the corresponding ^1H NMR spectrum reveals distinguishable chemical shifts as standard $(^{15}\text{NH}_4)_2\text{SO}_4$ without obvious peaks for the ^{14}N triplet, demonstrating that the detected ammonia completely derived from the supplied $^{15}\text{N}_2$.

To further evaluate the reaction kinetics of the $\text{CBC}/V_r\text{-ReSe}_2\text{@CBC}/\text{CBC}$ membrane as a NRR electrocatalyst, a series of electrocatalytic tests were conducted under different nitrogen flow rates and reaction temperatures. As shown in Figure 4c, both the NH_3 yield and Faradaic efficiency were maintained at almost unchanged values regardless of various nitrogen flow rates, indicating the N_2 diffusion process becomes a non-rate-determining step due to the existence of porous and hydrophobic CBC layers. Moreover, the NH_3 yield increases by 2.57 times when the NRR temperature increased from 0 °C to 60 °C (Figure 4d), which demonstrates that the mass transfer is a critical factor for accelerated NH_3 production rate by using $\text{CBC}/V_r\text{-ReSe}_2\text{@CBC}/\text{CBC}$ membrane as the electrocatalyst.

In accordance with the Arrhenius equation and Arrhenius plot (Figure S27), the apparent activation energy of CBC/V_r-ReSe₂@CBC/CBC membrane for NRR process is calculated as 12.1 kJ mol⁻¹, demonstrating its low energy cost as compared with the energy-intensive Haber-Bosch process.

To reveal the structural advantages of two-side hydrophobic layers for nitrogen bubble absorption, nitrogen bubble adhesive force measurements for both V_r-ReSe₂@CBC and CBC/V_r-ReSe₂@CBC/CBC membranes were investigated by using one nitrogen bubble (in 0.1M Na₂SO₄ electrolyte) to touch their under-electrolyte surfaces,^[42] respectively. As a result, there is only a weak adhesive force between the nitrogen bubble and the measured surface of V_r-ReSe₂@CBC membrane (Figure 5a) while a strong bubble adhesive force is measured on the surface of CBC/V_r-ReSe₂@CBC/CBC membrane (Figure 5 b), which is further demonstrated through the appreciable deformation of the nitrogen bubble during the corresponding measurement process (insets 1-3 of Figure 5). The bubble contact angles reach 140.9±2.1° and 137.7±2.3° on the surfaces of V_r-ReSe₂@CBC and CBC/V_r-ReSe₂@CBC/CBC membranes under electrolyte (insets 4), respectively. Additionally, surface superhydrophilicity of the V_r-ReSe₂@CBC membrane is shown in inset 5 of Figure 5a, when the infiltrated electrolyte droplet was immediately put into the membrane. Attributable to the protection from the CBC layers, the CBC/V_r-ReSe₂@CBC/CBC membrane processes a dramatically enhanced hydrophobicity (inset 5 of Figure 5b), which is beneficial to suppressing the hydrogen evolution reaction by restricting the contact between electrocatalytic V_r-ReSe₂@CBC interior and aqueous electrolyte. The abrupt three-phase interface provides a discontinuous state with abundant free electroactive sites for enhanced NRR process.

Furthermore, COMSOL Multiphysics simulations were performed to reveal the advantages of covered hydrophobic CBC layer by constructing a three-dimensional model in Figure S28a, where the V_r-ReSe₂@CBC was adhered on the one-side of hydrophobic and porous CBC layer with a cuboid shape (0.25 × 0.04 × 0.07 m). As shown in Figure S28b, the voltage and the H⁺ concentration in the right boundary of the model are fixed as 5.5 V and 0.1 mmol m⁻³, with continuous diffusion of H⁺ ions

from right to left boundaries for nitrogen reduction reactions. In detail, the COMSOL Multiphysics simulations were conducted by using secondary current distribution and transport of diluted species modules with more details in the Supporting Information. As plotted in Figure 6a, the voltage at the most left-band side boundary of the $V_r\text{-ReSe}_2\text{@CBC}$ interface maintains at a higher but stable value of ≈ 5.6 V, when the internal diffusion reaches to an equilibrium within 5.5 s of the reaction time. Meanwhile, the concentration of H^+ ions at the most left side boundary of the $V_r\text{-ReSe}_2\text{@CBC}$ interface is close to zero with the increase of reaction time (Figure 6b), indicating the fast hydrogen coupling process with nitrogen molecules to realize rapid ammonia production. The rapid equilibriums within 5.5 s for both the voltage and concentration of H^+ ions at the left-band side boundary of electrocatalytic $V_r\text{-ReSe}_2\text{@CBC}$ demonstrate the hydrophobic and porous CBC layer would not significantly affect the NRR process with plenty of N_2 source. Then, the distribution of various parameters in the electrode, including voltage, current density and concentration of H^+ ions, are shown in Figure 6c-6e when the reaction time is 5.5 s. The voltages in the boundary of the hydrophobic and porous CBC layer (right side of the model) and the left boundary of $V_r\text{-ReSe}_2\text{@CBC}$ interface are calculated to be 5.99 and 5.58 V [based on Equation (4) in the Supporting Information], respectively, with a slight difference of 0.41 V (Figure 6c). This slight voltage reduction is attributed to the high conductivity of the well-connected CBC nanofibers, which ensures enough supplied electrons to reduce nitrogen on the electrocatalytic $V_r\text{-ReSe}_2\text{@CBC}$ interface with low energy dissipation from internal resistance. Meanwhile, the current density near the electrocatalytic $V_r\text{-ReSe}_2\text{@CBC}$ interface is slightly higher than those in the right region of CBC layer (Figure 6d), where the arrow lines imply the direction of current density change. The narrow change of the current density is also attributed to the high conductivity of CBC nanofibers with enhanced NRR process near the $V_r\text{-ReSe}_2\text{@CBC}$ interface. The H^+ concentration near the interface of $V_r\text{-ReSe}_2\text{@CBC}$ decreases dramatically (Figure 6e), which indicates the possible resistance towards water molecules as the hydrophobic and porous properties for as-covered CBC layer on the top of $V_r\text{-ReSe}_2\text{@CBC}$. As a result, only limited electrolyte

could be in contact with the interface of electrocatalytically active $V_r\text{-ReSe}_2\text{@CBC}$, resulting in suppressed HER process with more unused active sites for NRR in the $\text{CBC}/V_r\text{-ReSe}_2\text{@CBC}/\text{CBC}$ membrane.

3. Conclusion:

In summary, we have prepared a “sandwich”-structured $\text{CBC}/V_r\text{-ReSe}_2\text{@CBC}/\text{CBC}$ membrane with hydrophobic surface and high electroactivity. As predicted by the DFT calculation results, the introduced selenium vacancy could modulate the electronic structures of ReSe_2 nanosheet by positively shifting its d-band position, which shows poor electrocatalytic selectivity with simultaneously enhanced NRR and HER processes. As revealed by the under-electrolyte nitrogen bubble adhesive force and superhydrophilic measurements, the covered hydrophobic CBC layer is beneficial to resisting the intimate contact between water molecules and $V_r\text{-ReSe}_2\text{@CBC}$ nanofibers, and slightly increases the adhesive force towards nitrogen bubbles. As a result, the $\text{CBC}/V_r\text{-ReSe}_2\text{@CBC}/\text{CBC}$ membrane displayed a boosted Faradaic efficiency by $\approx 32\%$ at room temperature. As revealed by COMSOL Multiphysics stimulations, the porous and hydrophobic CBC layers could provide special channels for sluggish internal diffusion of H^+ ions, leaving limited water molecules to contact the electro-active $V_r\text{-ReSe}_2\text{@CBC}$ nanofibers and more unoccupied active site for nitrogen adsorption and NRR processes. This work provides a possible strategy to ameliorate potentially active NRR catalysts by constructing a three-phase boundary at an abrupt interface.

Acknowledgements

We are grateful for the financial support from the National Natural Science Foundation of China (21674019, 51801075), the Shanghai Scientific and Technological Innovation Project (18JC1410600), the Program of Shanghai Academic Research Leader (17XD1400100), the Engineering and Physical Sciences Research Council (EPSRC, EP/L015862/1). J.H. and J.M. gratefully acknowledge the financial support of the Flemish Government through the Moonshot cSBO project P2C

(HBC.2019.0108) and through long-term structural funding (Methusalem). D.R. gratefully acknowledges the support of Jiangsu Overseas Visiting Scholar Program for University Prominent Young and Mid-aged Teachers and Presidents. Theoretical work was carried out at LvLiang Cloud Computing Center of China, and the calculations were performed on TianHe-2.

Received: ((will be filled in by the editorial staff))
Revised: ((will be filled in by the editorial staff))
Published online: ((will be filled in by the editorial staff))

References

-
- [1] J. W. Erisman, M. A. Sutton, J. Galloway, Z. Klimont, W. Winiwarter, *Nat. Geosci.* **2008**, *1*, 636-639.
- [2] B. M. Hoffman, D. Lukoyanov, Z. Y. Yang, D. R. Dean, L. C. Seefeldt, *Chem. Rev.* **2014**, *114*, 4041-4062.
- [3] M. A. Légaré, G. Blanger-Chabot, R. D. Dewhurst, E. Welz, I. Krummenacher, B. Engels, H. Braunschweig, *Science* **2018**, *359*, 896-900.
- [4] A. Klerke, C. H. Christensen, J. K. Nørskov, T. Vegge, *J. Mater. Chem.* **2008**, *18*, 2304-2310.
- [5] A. E. Shilov, *Russ. Chem. Bull.* **2003**, *52*, 2555-2562.
- [6] C. D. Lv, C. S. Yan, G. Chen, Y. Ding, J. X. Sun, Y. S. Zhou, G. H. Yu, *Angew. Chem. Int. Ed.* **2018**, *57*, 6073-6076; *Angew. Chem.* **2018**, *130*, 6181-6184.
- [7] J. N. Renner, L. F. Greenlee, A. M. Herring, K. E. Ayers, *Electrochem. Soc.* **2015**, *24*, 51-57.
- [8] C. J. M. van der Ham, M. T. M. Koper, D. G. H. Hetterscheid, *Chem. Soc. Rev.* **2014**, *43*, 5183-5191.
- [9] X. Chen, N. Li, Z. Kong, W. J. Ong, X. Zhao, *Mater. Horiz.* **2018**, *5*, 9-27.
- [10] K. C. Macleod, P. L. Holland, *Nat. Chem.* **2013**, *5*, 559-565.
- [11] C. Guo, J. Ran, A. Vasileff, S. Z. Qiao, *Energy Environ. Sci.* **2018**, *11*, 45-56.
- [12] Z. W. Seh, J. Kibsgaard, C. F. Dickens, I. Chorkendorff, J. K. Nørskov, T. F. Jaramillo, *Science* **2017**, *355*, eaad4998.

- [13] M. A. Shipman, M. D. Symes, *Catal. Today* **2017**, 286, 57-68.
- [14] K. H. Liu, H. X. Zhong, S. L. Li, Y. X. Duan, M. M. Shi, X. B. Zhang, J. M. Yan, Q. Jiang, *Prog. Mater. Sci.* **2018**, 92, 64-111.
- [15] S. Licht, B. Cui, B. Wang, F.-F. Li, J. Lau, S. Liu, *Science* **2014**, 345, 637-640.
- [16] G.-F. Chen, X. Cao, S. Wu, X. Zeng, L.-X. Ding, M. Zhu, H. Wang, *J. Am. Chem. Soc.* **2017**, 139, 9771-9774.
- [17] H. P. Jia, E. A. Quadrelli, *Chem. Soc. Rev.* **2014**, 43, 547-564.
- [18] S. Chen, S. Perathoner, C. Ampelli, C. Mebrahtu, D. Su, G. Centi, *Angew. Chem. Int. Ed.* **2017**, 56, 2699-2703; *Angew. Chem.* **2017**, 129, 2743-2747.
- [19] L. M. Azofra, N. Morlanés, A. Poater, M. K. Samantaray, B. Vidjayacoumar, K. Albahily, L. Cavallo, J.-M. Basset, *Angew. Chem. Int. Ed.* **2018**, 57, 15812-15816; *Angew. Chem.* **2018**, 130, 16038-16042.
- [20] Y. Yao, S. Zhu, H. Wang, H. Li, M. Shao, *J. Am. Chem. Soc.* **2018**, 140, 1496-1501.
- [21] F. L. Lai, N. Chen, X. B. Ye, G. J. He, W. Zong, K. B. Holt, B. C. Pan, I. P. Parkin, T. X. Liu, R. J. Chen, *Adv. Funct. Mater.* **2020**, 30, 1907376.
- [22] H. Cheng, L.-X. Ding, G.-F. Chen, L. L. Zhang, J. Xue, H. H. Wang, *Adv. Mater.* **2018**, 30, 1803694.
- [23] X. H. Li, T. S. Li, Y. J. Ma, Q. Wei, W. B. Qiu, H. R. Guo, X. F. Shi, P. Zhang, A. M. Asiri, L. Chen, B. Tang, X. P. Sun, *Adv. Energy Mater.* **2018**, 8, 1801357.
- [24] E. Skúlason, T. Bligaard, S. Gudmundsdóttir, F. Studt, J. Rossmeisl, F. Abild-Pedersen, T. Vegge, H. Jónsson, J. K. Nørskov, *Phys. Chem. Chem. Phys.* **2012**, 14, 1235-1245.
- [25] H. K. Lee, C. S. L. Koh, Y. H. Lee, C. Liu, I. Y. Phang, X. M. Han, C.-K. Tsung, X. Y. Ling, *Sci. Adv.* **2018**, 4, eaar3208.
- [26] J. F. Xie, H. Zhang, S. Li, R. X. Wang, X. Sun, M. Zhou, J. F. Zhou, X. W. Lou, Y. Xie, *Adv. Mater.* **2013**, 25, 5807-5813.

- [27] J. F. Xie, J. J. Zhang, S. Li, F. Grote, X. D. Zhang, H. Zhang, R. X. Wang, Y. Lei, B. C. Pan, Y. Xie, *J. Am. Chem. Soc.* **2013**, *135*, 17881-17888.
- [28] Q. Zhang, W. J. Wang, X. Kong, R. G. Mendes, L. W. Fang, Y. H. Xue, Y. Xiao, M. H. Rummeli, S. L. Chen, L. Fu, *J. Am. Chem. Soc.* **2016**, *138*, 11101-11104.
- [29] V. Babentsov, R. B. James, *J. Cryst. Growth* **2013**, *379*, 21-27.
- [30] D. J. Keeble, E. A. Thomsen, A. Stavrinadis, I. D. W. Samuel, J. M. Smith, A. A. R. Watt, *J. Phys. Chem. C* **2009**, *113*, 17306-17312.
- [31] Y. Sun, J. Meng, H. X. Ju, J. F. Zhu, Q. X. Li, Q. Yang, *J. Mater. Chem. A* **2018**, *6*, 22526-22533.
- [32] A. J. Almeida, A. Sahu, A. Riedinger, D. J. Norris, M. S. Brandt, M. Stutzmann, R. N. Pereira, *J. Phys. Chem. C* **2016**, *120*, 13763-13770.
- [33] Z. Y. Wu, D. C. Xian, T. D. Hu, Y. N. Xie, Y. Tao, C. R. Natoli, E. Paris, A. Marcelli, *Phys. Rev. B* **2004**, *70*, 033104.
- [34] F. Hilbrig, C. Michel, G. L. Haller, *J. Phys. Chem.* **1992**, *96*, 9893.
- [35] M. Fręba, K. Lochte, W. Metz, *J. Phys. Chem. Solids* **1996**, *57*, 635.
- [36] D. E. Sayers, E. A. Stern, F. W. Lytle, *Phys. Rev. Lett.* **1971**, *27*, 1204.
- [37] Z. Sun, Q. Liu, T. Yao, W. Yan, S. Q. Wei, *Sci. China Mater.* **2015**, *58*, 313-341.
- [38] C. L. Tan, Z. M. Luo, A. Chaturvedi, Y. Q. Cai, Y. H. Du, Y. Gong, Y. Huang, Z. C. Lai, X. Zhang, L. R. Zheng, X. Y. Qi, M. H. Goh, J. Wang, S. K. Han, X.-J. Wu, L. Gu, C. Kloc, H. Zhang, *Adv. Mater.* **2018**, *30*, 1705509.
- [39] H. Funke, A. Scheinost, M. Chukalina, *Phys. Rev. B* **2005**, *71*, 094110.
- [40] H. K. Lee, Y. H. Lee, J. V. Morabito, Y. Liu, C. S. L. Koh, I. Y. Phang, S. Pedireddy, X. Han, L.-Y. Chou, C.-K. Tsung, X. Y. Ling, *J. Am. Chem. Soc.* **2017**, *139*, 11513-11518.
- [41] A. Quinn, R. Sedev, J. Ralston, *J. Phys. Chem. B* **2003**, *107*, 1163-1169.
- [42] Y. Huang, M. J. Liu, J. X. Wang, J. M. Zhou, L. B. Wang, Y. L. Song, L. Jiang, *Adv. Funct. Mater.* **2011**, *21*, 4436-4441.

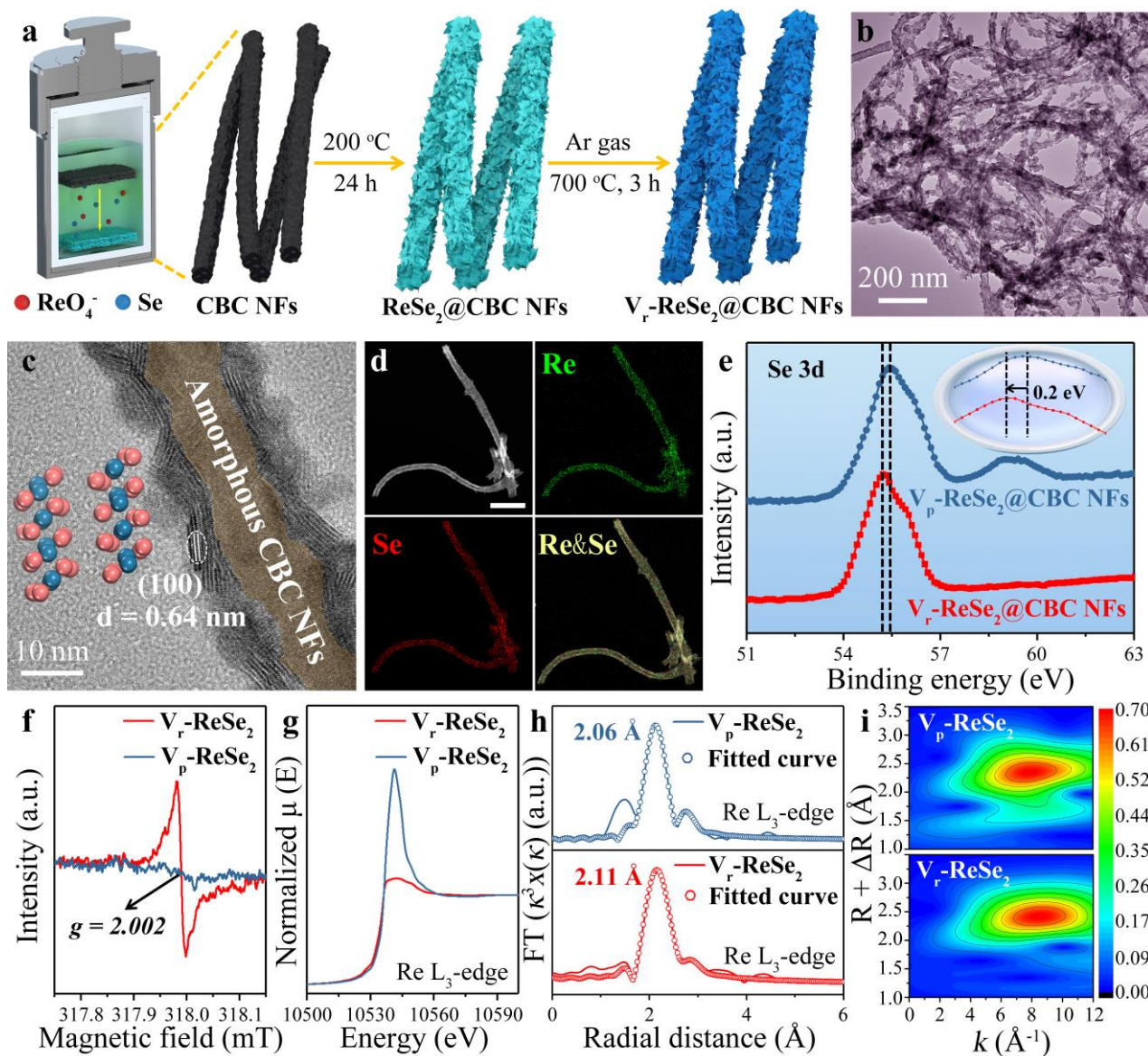


Figure 1. a) Illustration of the fabrication of $V_r\text{-ReSe}_2\text{@CBC NFs}$. b) TEM, and c) HRTEM images for $V_r\text{-ReSe}_2\text{@CBC NFs}$. The light-coral and blue balls present Se and Re, respectively. d) HAADF and corresponding EDX elemental mapping images for $V_r\text{-ReSe}_2\text{@CBC NFs}$. The scale-bar is 200 nm. e) High resolution spectra of Se 3d region for $V_p\text{-ReSe}_2\text{@CBC}$ and $V_r\text{-ReSe}_2\text{@CBC NFs}$. f) EPR spectra, g) Re L_3 -edge XANES spectra, h) corresponding FT-EXAFS spectra, and i) WT-EXAFS for $V_p\text{-ReSe}_2$ and $V_r\text{-ReSe}_2$ nanosheets.

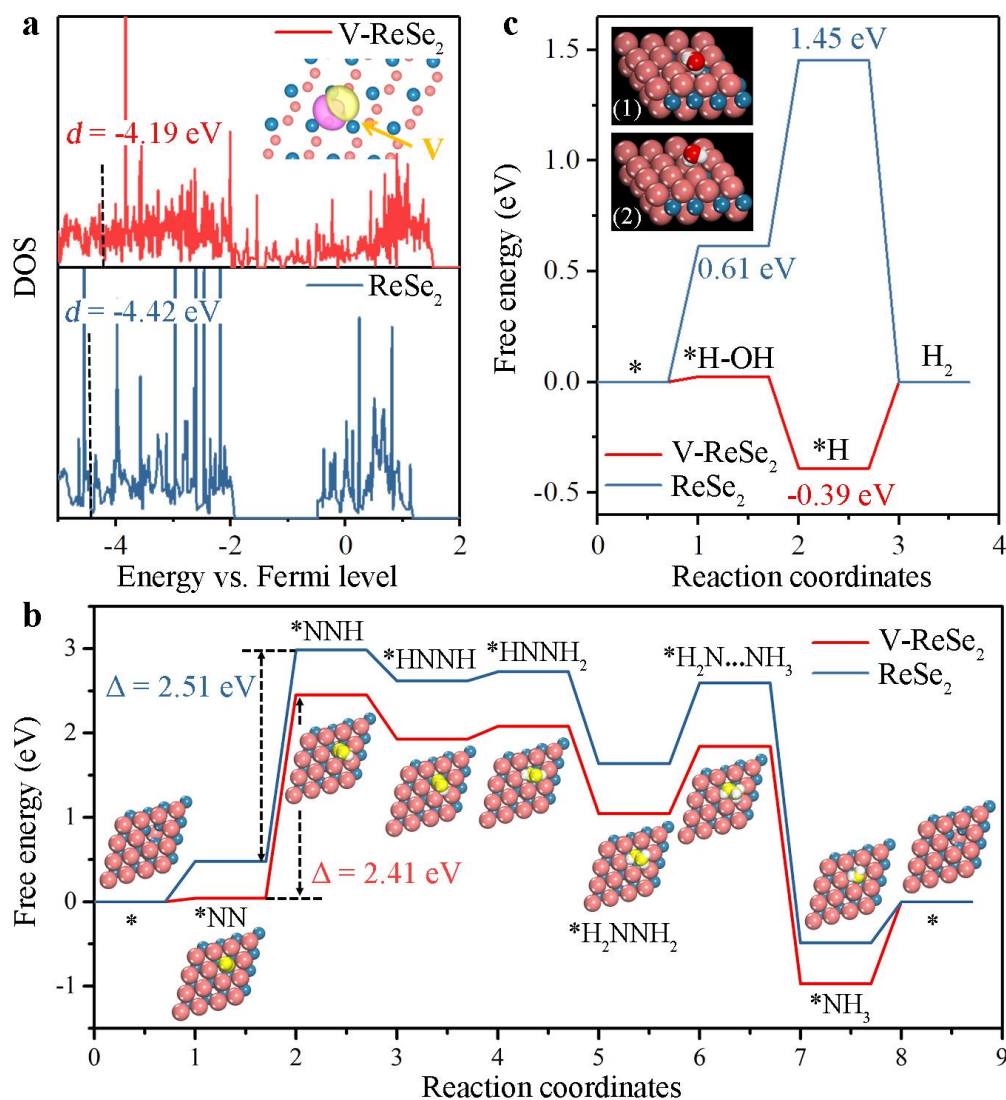


Figure 2. a) Density of states (DOS) for V-ReSe₂ and ReSe₂ models, as well as the charge density difference of V-ReSe₂. Here, the pink and yellow areas present electrons accumulation and depletion, respectively. b) Free energy diagrams for nitrogen reduction reaction on the surface of V-ReSe₂ and ReSe₂ catalysts. The insets show the optimized structures on V-ReSe₂ surface during electrocatalytic process. c) Free energy diagrams for hydrogen evolution reaction on the surface of V-ReSe₂ and ReSe₂ catalysts. The insets show the optimized structures of water adsorption on V-ReSe₂ and ReSe₂ surfaces. Here, the adsorption site is denoted by an asterisk (*). The light-coral, blue, yellow, white, and red balls present Se, Re, N, H, and O atoms, respectively.

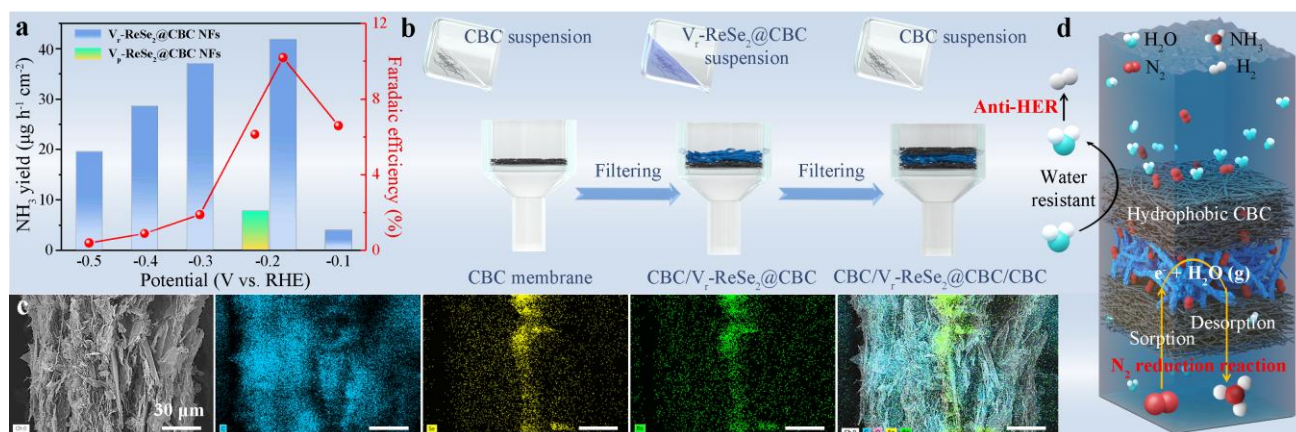


Figure 3. a) Electrocatalytic NRR performance with NH₃ yield (bar graph) and Faradaic efficiency (red point) for V_r-ReSe₂@CBC and V_p-ReSe₂@CBC NFs in 0.1M Na₂SO₄ electrolyte under ambient conditions. b) Schematic illustration for the preparation of “sandwich”-structured CBC/V_r-ReSe₂@CBC/CBC membrane. c) EDX elemental mapping images of CBC/V_r-ReSe₂@CBC/CBC membrane with C, Se, Re, and mixed elements. The scale bar: 30 μm. d) Proposed overall mechanism for the selective and enhanced electrochemical NRR process by encapsulating V_r-ReSe₂@CBC NFs within hydrophobic CBC layers.

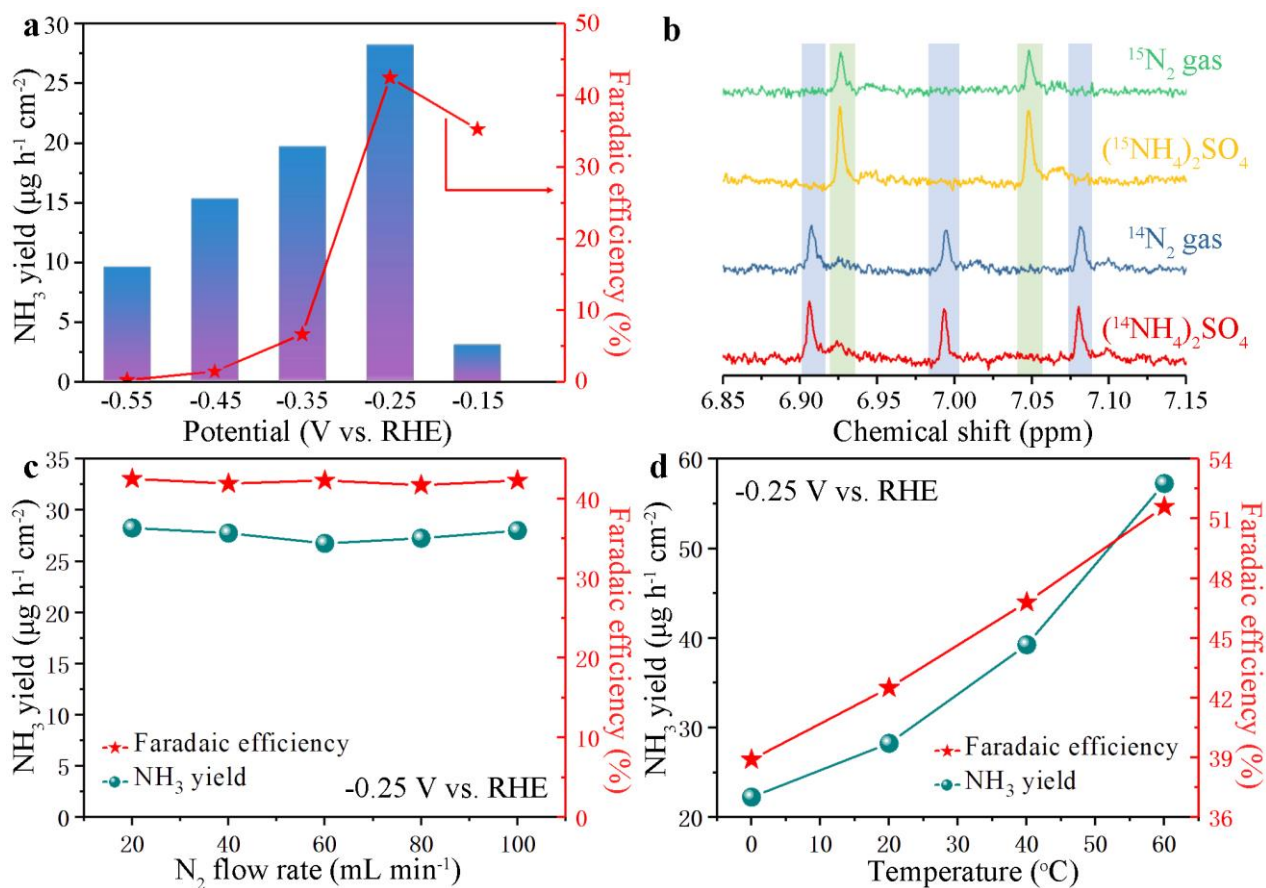


Figure 4. a) Electrocatalytic NRR performance with NH₃ yield (bar graph) and Faradaic efficiency (red star) for CBC/V_r-ReSe₂@CBC/CBC membrane under ambient condition. b) ¹H NMR analysis of the membrane fed by ¹⁴N₂ and ¹⁵N₂ gases after electrochemical NRR process. NH₃ yield and Faradaic efficiency under c) different N₂ flow rates and d) temperatures at -0.25 V vs. RHE.

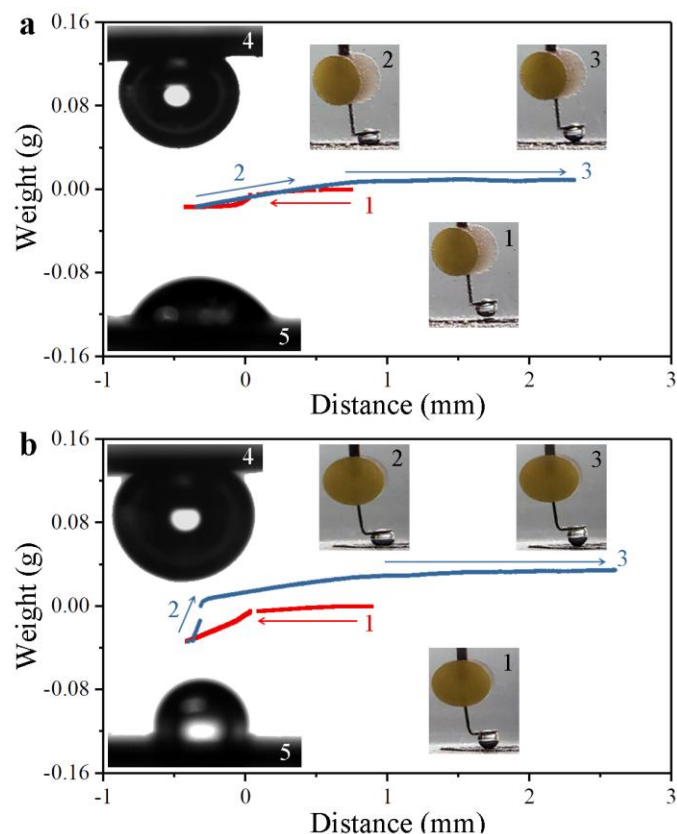


Figure 5. Under-electrolyte (0.1M Na₂SO₄) nitrogen bubble adhesive force and superhydrophilic measurements. a,b) Nitrogen bubble adhesive force measurements of V_r-ReSe₂@CBC and CBC/V_r-ReSe₂@CBC/CBC membranes. The V_r-ReSe₂@CBC membrane obviously shows weak bubble adhesive force (≈ 32 mg) while the strong bubble adhesive force is measured on CBC/V_r-ReSe₂@CBC/CBC membrane (≈ 88 mg). The insets 1-3 show different bubble states during the corresponding measurement process for adhesive force, where process 1 displays the nitrogen bubble gets close to the electrode surface, process 2 illustrates the nitrogen bubble touches with electrode surface, and process 3 demonstrates the nitrogen bubble separates from the electrode surface, respectively. The nitrogen bubble contact angles under electrolyte were measured as $140.9 \pm 2.1^\circ$ and $137.7 \pm 2.3^\circ$ for V_r-ReSe₂@CBC and CBC/V_r-ReSe₂@CBC/CBC membranes (insets 4), respectively. For inset 5, the wetting ability of the membranes in Na₂SO₄ solution droplets demonstrates the surface hydrophobicity of CBC/V_r-ReSe₂@CBC/CBC membrane.

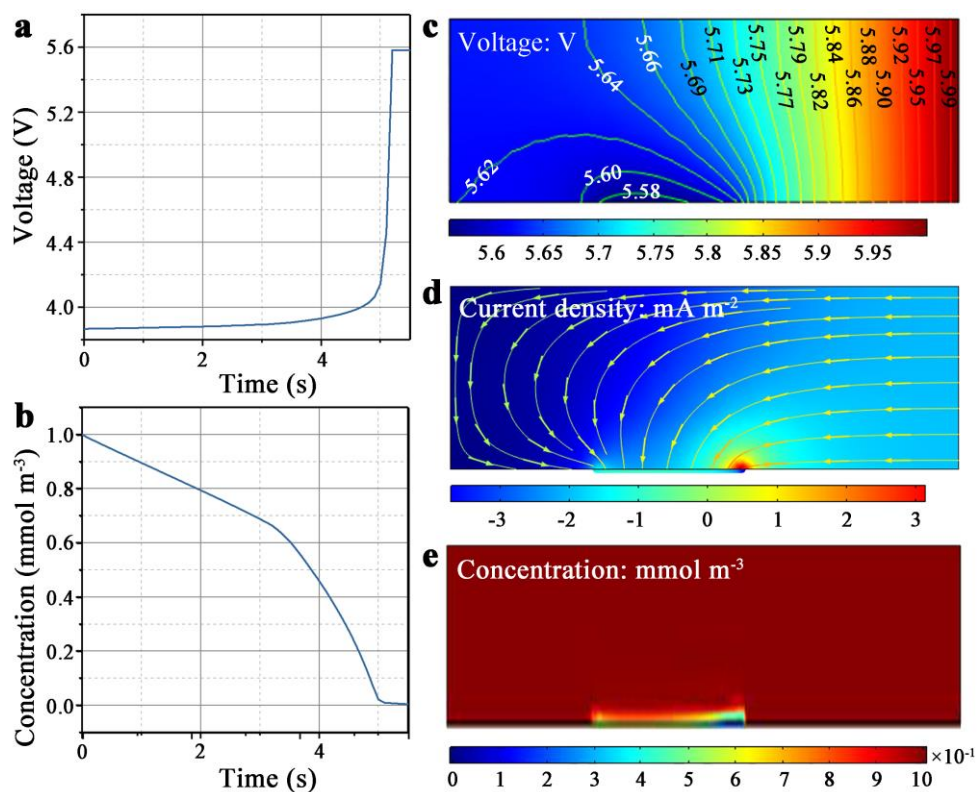


Figure 6. The changes of a) voltage and b) concentration (H^+ ions) in the simulated electrodes with a hydrophobic and porous surface within 5.5 s in the most left boundary of the $\text{V}_r\text{-ReSe}_2\text{@CBC}$. The distributions of c) voltage, d) current density, and e) concentration of H^+ ions in the electrode when the reaction time is 5.5 s.